Journal of Power Sources 196 (2011) 3485–3495

Contents lists available at ScienceDirect

Journal of Power Sources

journal homepage: www.elsevier.com/locate/jpowsour

Power generation enhancement of solid oxide fuel cell by cathode–electrolyte interface modification in mesoscale assisted by level set-based optimization calculation

Hiroshi Iwai[a,*], Atsushi Kuroyanagi[a], Motohiro Saito[a], Akio Konno[a], Hideo Yoshida[a], Takayuki Yamada[b], Shinji Nishiwaki[b]

[a] Department of Aeronautics and Astronautics, Kyoto University, Sakyo-ku, Kyoto 606-8501, Japan
[b] Department of Mechanical Engineering and Science, Kyoto University, Sakyo-ku, Kyoto 606-8501, Japan

ARTICLE INFO

Article history:
Received 11 September 2010
Received in revised form
16 November 2010
Accepted 10 December 2010
Available online 21 December 2010

Keywords:
Solid oxide fuel cell
Cathode–electrolyte interface
Optimization calculation
Numerical prediction
Mesoscale structure control

ABSTRACT

To explore potential for the power density enhancement of solid oxide fuel cells by controlling the cathode–electrolyte interface in mesoscale, two-dimensional numerical simulations were conducted. In the simulation, a level set-based topology optimization technique was successfully coupled with the SOFC simulation based on a microscale model and was applied for the local optimization of the interface shape. The numerical results showed that the optimized shape of the cathode–electrolyte interface varied depending on the simulation conditions and that the cell performance could be improved by applying non-flat design to the cathode–electrolyte interface for the same amount of cathode/electrolyte materials.

1. Introduction

Fuel cells are devices which directly convert the chemical energy of reactants into electricity through electrochemical reactions. Among various fuel cell types, the solid oxide fuel cell (SOFC) has recently been attracting particular attention for its high efficiency and fuel flexibility [1]. One of the unique features of SOFCs is that all components in an SOFC system are solid, including the ceramic electrolyte, which permits exceptional geometrical flexibility of the cell design. By controlling the cell's macroscopic shape, we can achieve designs that offer select advantages. For example, a tubular type of cell has good resistance to thermal stress while planar, or flattened-tubular types, can be stacked compactly to provide high power density [2,3]. A micro-tubular type of cell is mechanically strong and can achieve the high power densities suitable for small applications [4,5]. Geometry control is a challenging topic when designing the porous electrodes of a SOFC. It is widely recognized that the electrode microstructure has a significant impact on cell performance as well as cell durability [6–10]. Therefore, quantification of the porous microstructure and its correlation to the cell performance are the recent interests [11,12]. These porous electrodes must have appropriate microstructures that increase the density of reaction sites, reduce resistance to gas diffusion and establish efficient networks of both ion and electron conductors. Unlike the direct control of geometry in the macroscale, the electrode microstructure is usually controlled indirectly and statistically. Composite electrode (e.g., LSM–YSZ) is an example of microstructure control commonly used in SOFC [13]. Following recent understanding that electrochemical reaction proceeds most prominently near the electrode–electrolyte interface, the microstructure control within this effective thickness of the electrode is gathering attention. Reports on the surface roughness of the interface can be found in literature [14,15]. Use of nanoparticles near the interface to increase the number of reaction sites is also an example of a microstructure modification [16–18]. However, this approach currently encounters durability problems in long-term use [9,10,19].

Konno et al. [20] recently investigated the possibility of the electrode–electrolyte interface shape modification to increase the interface area and consequently the active reaction region in the electrode. The order of the structure scale in the study was about 10–100 μm so that the characteristic length of the structure became larger than the effective thickness of the electrode. The effects of this "mesoscale" structure on Ni–YSZ anode performance were examined numerically and experimentally and positive conclusions were obtained on this concept. It is worth noting that a

* Corresponding author. Tel.: +81 75 7535218; fax: +81 75 7535203.
E-mail address: iwai.hiroshi.4x@kyoto-u.ac.jp (H. Iwai).

0378-7753/$ – see front matter © 2010 Elsevier B.V. All rights reserved.
doi:10.1016/j.jpowsour.2010.12.024

Nomenclature

D_{ij}	binary diffusivity ($m^2\ s^{-1}$)
D_{iK}	Knudsen diffusivity ($m^2\ s^{-1}$)
d	particle diameter (m)
E_0	*EMF* at the standard state (V)
F	Faraday constant ($C\ mol^{-1}$)
I_{tpb}	charge transfer current ($A\ m^{-3}$)
i	current density ($A\ m^{-2}$)
i_{tpb}	charge transfer current per TPB length ($A\ m^{-1}$)
K	permeability
l_{tpb}	TPB density (m^{-2})
P	percolation probability
p	partial pressure (Pa)
R	universal gas constant ($J\ mol^{-1}\ K^{-1}$)
T	temperature (K)
V	volume fraction
V_{max}	upper limit of volume constraint (m^3)

Greek letters

ε	porosity of porous electrode
ϕ	potential (V)
ϕ_0	Nernst potential (electromotive force) (V)
ϕ_{FC}	cell terminal voltage (V)
γ	coefficient of complexity
η	overpotential (V)
σ	conductivity ($S\ m^{-1}$)
τ	tortuosity factor

Subscripts

A	anode
act	activation
ave	average
C	cathode
E	electrolyte
el	electronic conducting material
io	ionic conducting material
tpb	three-phase boundary
∞	bulk gas phase

geometry control of this scale has some advantages over macroscopic or microscopic scales. Because the structure is large enough compared to the microstructure of the porous electrode, it is free from the durability problem caused by the morphology change. Precision fabrication of the designed interface shape is possible as well. On the other hand, the structure is small enough compared to the macroscopic cell shape that it can be applied in a variety of cell types (e.g., tubular and planar).

An effective design of the electrode–electrolyte interface is not clear yet because the effectiveness of the interface shape control in mesoscale depends on various resistances in the cell and the operation condition. For such design problem, there is a possibility that an optimization calculation technique can be efficiently used. In this paper, to explore the potential for power density enhancement through mesoscale interface control, we perform two-dimensional numerical simulations of a SOFC where a level set-based topology optimization technique [21] is applied for the local optimization of the interface shape.

2. Concept of shape modification of the electrode–electrolyte interface

The electrochemical reactions proceed at the three-phase boundary (TPB) where the ion conductor, electron conductor and gas phase meet. TPBs are distributed in the porous electrodes but it is reported that they are not equally active, that the electrochemical reactions occur more prominently near the electrode–electrolyte interface [22,23]. Thus the most effective thickness of electrodes is an open question, but in this section, for simplicity, we assume that the electrochemical reactions take place only at the interface.

Fig. 1 schematically shows the concept of an interface modification, taking the cathode side as an example. If the interface has a wavy shape as shown in Fig. 1(b), the interface area is increased compared to the flat case (Fig. 1(a)), which implies that the electrochemically active region is enlarged by the wavy shape. At the position marked "A" in Fig. 1(b), the electrolyte thickness is reduced while the cathode thickness is increased. This means that the potential loss associated with ion transfer in the electrolyte is reduced, but the concentration overpotential is increased. At position "B", an opposite situation is obtained. The overall performance of the cell is determined by the sum of all these effects.

We further simplify the problem by neglecting the concentration overpotential because its effect is usually minor in a practical cell operating under normal conditions. Then the performance of a flat cell (Fig. 1(a)) can be described by the balance between the ion transfer resistance in the electrolyte and the reaction resistance at the interface. Konno et al. [20] introduced a non-dimensional number, Bi_{FC}, as follows:

$$Bi_{FC} = \frac{ASR_{electrolyte}}{ASR_{reaction}} = \frac{1/ASR_{reaction}}{1/ASR_{electrolyte}} = \frac{1/ASR_{reaction}}{\sigma_{electrolyte}/l_{electrolyte}} \quad (1)$$

ASR, $\sigma_{electrolyte}$, and $l_{electrolyte}$ are the area specific resistance, ion conductivity of the electrolyte, and electrolyte thickness, respectively. $ASR_{reaction}$ can be expressed in terms of the activation overpotential and the current density.

$$ASR_{reaction} = \frac{\eta_{act}}{i} \quad (2)$$

When Bi_{FC} is larger than unity, ion transport is the dominant phenomenon and expansion of the interface area becomes ineffective. Expansion of the interface area can be effective when Bi_{FC} is less than unity, where the reaction resistance is the bottleneck. The value of Bi_{FC} is affected by the choice of electrolyte materials, electrolyte thickness, temperature, current density and microstructure of the electrode. We assume a cell made of Yttria Stabilized Zirconia (YSZ) electrolyte and Lanthanum Strontium Manganate (LSM) cathode and estimate the value of Bi_{FC}. $\sigma_{electrolyte}$ and η_{act} are estimated following Bessette et al. [24] and Costamagna and Honegger [25], respectively. Bi_{FC} values for different electrolyte thicknesses and temperatures are shown in Fig. 2. The current density is fixed at $300\ mA\ cm^{-2}$. Bi_{FC} can assume values less than 1, especially when the electrolyte is thin. Considering that the electrolyte thicknesses of today's electrode-supported cells are typically in the range of 10–20 μm, Fig. 2 indicates the possibility of power density enhancement by shape modification of the electrode–electrolyte interface.

The above discussion by Bi_{FC} is based on the assumption that the electrochemical reactions proceed at the electrode–electrolyte interface. The effect of concentration overpotential is also neglected. In reality, the cell performance is affected by the ionic resistivity in electrolyte, ionic and electronic resistivity in electrode, electrode reaction resistivity and gas diffusion. To consider these effects, we perform numerical simulation and the results are reported in the following sections. Although interface modification is expected to be particularly effective when the electrolyte is thin as shown in Fig. 2, electrolyte-supported cells with thick electrolytes are used in this study. Bi_{FC} of the cell assumed in the following simulation is about 4, so the ion transfer resistance in the electrolyte is the major resistance of the cell. By using an electrolyte-supported cell, we can limit the shape modification

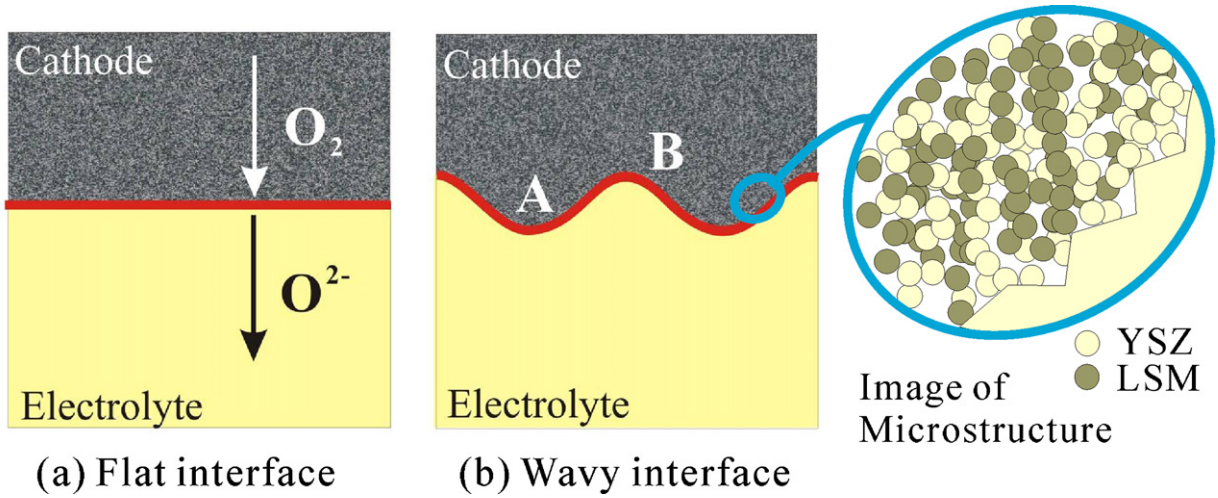

Fig. 1. Image of electrolyte–electrode interface transformation.

to only one side of the cell (the cathode) without affecting the shape of the other side (the anode). This is ideal for discussion in this study because we can avoid simultaneous modification of the two interfaces, namely, the cathode–electrolyte interface and the anode–electrolyte interface. It should be noted that our goal in this study is not to develop high power density cells, but to obtain fundamental information on how interface modification affects the cell's power density, and to clarify if this is a promising technique for developing more advanced SOFCs.

3. Numerical procedure

Fig. 3 shows a schematic view of the cell considered in this study. It is an electrolyte-supported cell, and the relatively thick electrolyte is sandwiched between anode and cathode electrodes. The electrolyte, anode and cathode materials are assumed to be YSZ, Ni–YSZ cermet and LSM–YSZ composite, respectively. In this study, an optimization calculation is implemented into the SOFC power generation simulation. The computational domain for the SOFC power generation covers all anode, electrolyte and cathode layers while the computational domain for the optimization calculation is limited to a half cell region including only the cathode and upper half of the electrolyte, as shown in Fig. 3. The width of the computational domain is set to 50 μm to appropriately limit the computational load. The following assumptions were made for simplification. The problem was assumed to be two-dimensional and steady. An isothermal condition was applied, assuming a constant temperature of 800 °C. The microstructure of the porous electrodes was modeled by the random packing of spheres with a constant and uniform particle diameter for both ionic and electronic conductors in the electrodes. Based on these assumptions, a numerical calculation program was developed. The next section describes an overall picture of the numerical model for the SOFC power generation prediction, followed by a section describing the optimization method applied to the cathode side of the cell in this study.

3.1. Simulation of SOFC power generation

3.1.1. Electrode microscale model

We adopted the microscale model proposed by Nam and Jeon [26] and extended it to a 2D simulation. This model calculates the charge transfer current at the three-phase boundary from the volume and area specific lengths of the three-phase boundary evaluated by a model based on random packing of spheres, and empirical correlations for the charge transfer current density based on experiments with patterned mesh electrodes. The anode and cathode charge transfer current density for a unit length of the three-phase boundary proposed in Ref. [26] are derived from the experiments of Bieberle et al. [27] and Radhakrishnan et al. [28], respectively, and expressed as

$$(i_{tpb})_A = \frac{\eta_{act}}{1.645 p_{H_2}^{-0.11} p_{H_2O}^{-0.67} \exp(10,212/T) \times 10^{-4\eta_{act}}}, \quad (3)$$

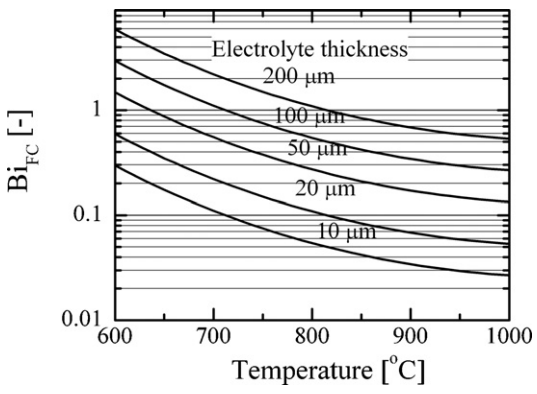

Fig. 2. Bi_{FC} estimation for YSZ electrolyte and LSM cathode system at an average current density of 300 mA cm^{-2}.

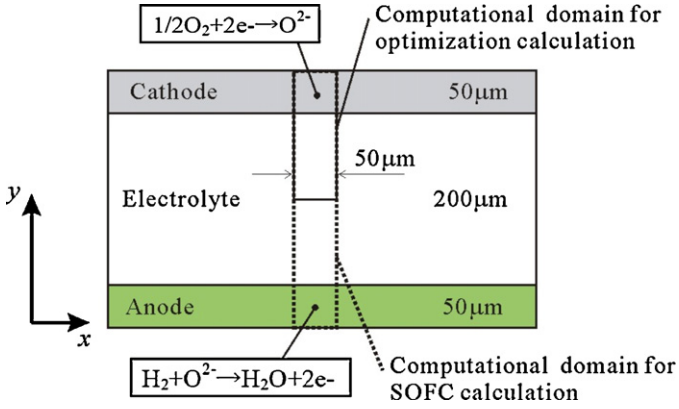

Fig. 3. Computational domains for the SOFC calculation and for the optimization calculation.

Table 1
Geometric parameters of electrode microscale structure.

	Value
$\varepsilon_A, \varepsilon_C$	0.3
τ_A, τ_C	3
$(V_{el})_A, (V_{el})_C$	0.5
$(V_{io})_A, (V_{io})_C$	0.5
$(n_{el})_A, (n_{el})_C$	0.5
$(n_{io})_A, (n_{io})_C$	0.5
$(d_{el})_A, (d_{el})_C$	1 μm
$(d_{io})_A, (d_{io})_C$	1 μm
θ_c	30°

$$(i_{tpb})_C = \frac{RT}{4F}\frac{2\sinh(2F\eta_{act}/RT)}{0.00136p_{O_2}^{-0.25}\exp(17,401/T)}, \tag{4}$$

where η_{act} is the activation overpotential and p_i is the partial pressure of species i. The charge transfer current is calculated as

$$I_{tpb} = i_{tpb}l_{tpb}, \tag{5}$$

where l_{tpb} is the density of the three-phase boundary per unit volume. It is evaluated by the random packing model using values for porosity, ε; tortuosity factor, τ; volume ratio of ion and electron conductors, V_{el},V_{io}; number density of ion and electron conductors, n_{el},n_{io}; particle diameter of ion and electron conductors, d_{el},d_{io}; contact angle of the particles, θ_c; as shown in Table 1.

The activation overpotential is calculated as

$$(\eta_{act})_A = (\phi_{el} - \phi_{io}) + \frac{RT}{2F}\ln\left(\frac{p_{H_2}}{p_{H_2,\infty}}\frac{p_{H_2O,\infty}}{p_{H_2O}}\right) \tag{6}$$

$$(\eta_{act})_C = (\phi_{io} - \phi_{el}) + \frac{RT}{4F}\ln\left(\frac{p_{O_2}}{p_{O_2,\infty}}\right) \tag{7}$$

The last term of the right-hand side of Eqs. (6) and (7) corresponds to the concentration overpotential. Equations (3), (4), (6) and (7) determine the electrochemical reaction rates for a given condition including the ionic and electronic potentials and gas concentrations.

3.1.2. Charge transfer and gas diffusion model

The ionic and electronic conductivities (S cm^{-1}) of the electrode and electrolyte bulk materials are obtained following expressions reported in literature [24,26,29,30].

$$\sigma^0_{YSZ} = \left(0.00294\exp\left(\frac{10,350}{T}\right)\right)^{-1} \tag{8}$$

$$\sigma^0_{LSM} = \frac{4.2\times10^5}{T}\exp\left(\frac{-1200}{T}\right) \tag{9}$$

$$\sigma^0_{Ni} = 3.27\times10^4 - 10.653T \tag{10}$$

The effective ionic or electronic conductivities in the porous electrode are expressed as

$$\sigma_i = \sigma_i^0[(1-\varepsilon)V_iP_i]^{1.5}, \tag{11}$$

where P_i is the percolation probability calculated through the random packing model. The effective conductivities are summarized in Table 2. The effective electronic conductivity is significantly large compared to the effective ionic conductivity. Therefore, we assume a uniform electronic potential in both electrodes and consider only the transport of ions and mass in the following computational model.

Table 2
Effective conductivity of electrodes.

	Anode	Cathode
σ_{io} (S cm^{-1})	4.1×10^{-3}	4.1×10^{-3}
σ_{el} (S cm^{-1})	3.6×10^{3}	2.4×10^{2}

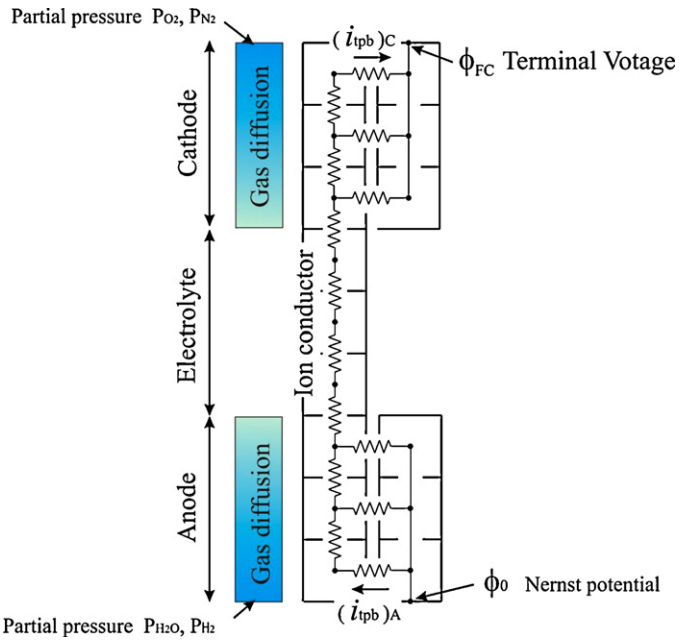

Fig. 4. Equivalent circuit model in one dimension.

Fig. 4 schematically shows the equivalent circuit model in one-dimensional geometry. Both ion transport and gas diffusion are considered in the electrodes while only ion transport takes place in the electrolyte. The governing equation for ion transport is expressed as

$$\frac{\partial}{\partial x}\left(\sigma_{io}\frac{\partial\phi_{io}}{\partial x}\right) + \frac{\partial}{\partial y}\left(\sigma_{io}\frac{\partial\phi_{io}}{\partial y}\right) = BI_{tpb}$$
$$B = \begin{cases} -1 & \text{Anode} \\ 0 & \text{Electrolyte} \\ +1 & \text{Cathode} \end{cases} \tag{12}$$

The term in the right-hand side is associated with the charge transfer between the ion conductive phase and the electron conductive phase. It is evaluated using the microscale model shown in the previous section.

For the mass transport in the anode, the dusty-gas model is adopted [31–33]. This model includes the diffusion flow and the viscous flow and is derived from Maxwell–Stefan equations considering the effect of Knudsen diffusion and Darcy's law. The governing equations can be expressed as

$$\frac{\partial}{\partial x}\left(\frac{k_{H_2}}{RT}\frac{\partial p_{H_2}}{\partial x}\right) + \frac{\partial}{\partial y}\left(\frac{k_{H_2}}{RT}\frac{\partial p_{H_2}}{\partial y}\right) + \frac{\partial}{\partial x}\left(\frac{k_Dp_{H_2}}{RT}\frac{\partial p_t}{\partial x}\right) + \frac{\partial}{\partial y}\left(\frac{k_Dp_{H_2}}{RT}\frac{\partial p_t}{\partial y}\right) = \frac{I_{tpb}}{2F}, \tag{13}$$

$$\frac{\partial}{\partial x}\left(\frac{k_{H_2O}}{RT}\frac{\partial p_{H_2O}}{\partial x}\right) + \frac{\partial}{\partial y}\left(\frac{k_{H_2O}}{RT}\frac{\partial p_{H_2O}}{\partial y}\right) + \frac{\partial}{\partial x}\left(\frac{k_Dp_{H_2O}}{RT}\frac{\partial p_t}{\partial x}\right) + \frac{\partial}{\partial y}\left(\frac{k_Dp_{H_2O}}{RT}\frac{\partial p_t}{\partial y}\right) = -\frac{I_{tpb}}{2F} \tag{14}$$

$$k_{H_2} = \frac{D^{eff}_{H_2-H_2O}D^{eff}_{H_2,K}}{D^{eff}_{H_2-H_2O} + D^{eff}_{m,K}}, \qquad k_{H_2O} = \frac{D^{eff}_{H_2-H_2O}D^{eff}_{H_2O,K}}{D^{eff}_{H_2-H_2O} + D^{eff}_{m,K}}$$

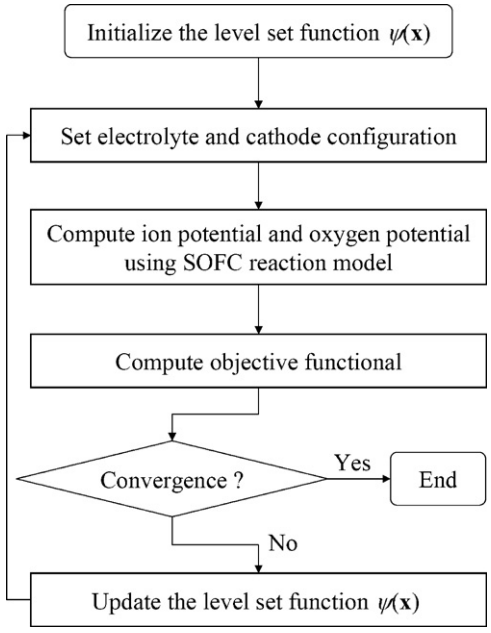

Fig. 5. Flowchart of the optimization calculation coupled with the SOFC simulation.

$$k_D = \frac{1}{p_t}\frac{D^{eff}_{H_2,K} D^{eff}_{H_2O,K}}{D^{eff}_{H_2-H_2O} + D^{eff}_{m,K}} + \frac{K}{\mu}$$

$$D^{eff}_{mK} = x_{H_2} D^{eff}_{H_2O,K} + x_{H_2O} D^{eff}_{H_2,K}$$

where p_t is total pressure, x_i is the molar fraction, and μ is the viscosity of the gas mixture. K is the permeability of the porous electrode, which is evaluated using the Carman–Kozeny relation [34] as

$$K = \frac{\varepsilon^3}{5(1-\varepsilon)^2(6/d)^2} \tag{15}$$

where d is the particle diameter of the ionic/electronic conductors. The mass transport in the cathode is evaluated as a self-diffusion of oxygen assuming the molar flux of nitrogen is zero [35]. The

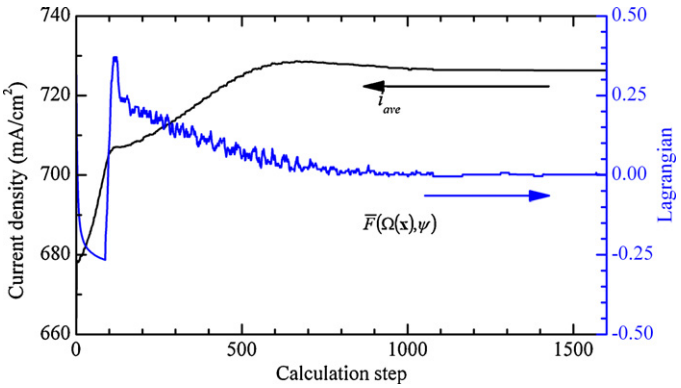

Fig. 7. Change in average current density and Lagrangian during optimization calculations.

governing equation is expressed as

$$\frac{\partial}{\partial x}\left(k_c \frac{\partial p_{O_2}}{\partial x}\right) + \frac{\partial}{\partial y}\left(k_c \frac{\partial p_{O_2}}{\partial y}\right) = \frac{I_{tpb}}{4F}$$
$$k_c = \frac{k_{O_2}}{1 - x_{O_2}\delta_{O_2}}\frac{1}{RT} \tag{16}$$
$$k_{O_2} = \frac{D^{eff}_{O_2-N_2} D^{eff}_{O_2,K}}{D^{eff}_{O_2-N_2} + D^{eff}_{O_2,K}} \qquad \delta_{O_2} = \frac{D^{eff}_{O_2,K}}{D^{eff}_{O_2-N_2} + D^{eff}_{O_2,K}}$$

The effective diffusivities for binary diffusion and Knudsen diffusion are affected by properties of the porous electrodes and are evaluated as

$$D^{eff}_{H_2-H_2O} = \frac{\varepsilon}{\tau} D_{H_2-H_2O}, \quad D^{eff}_{O_2-N_2} = \frac{\varepsilon}{\tau} D_{O_2-N_2}$$
$$D^{eff}_{H_2,K} = \frac{\varepsilon}{\tau} D_{H_2,K}, \quad D^{eff}_{H_2O,K} = \frac{\varepsilon}{\tau} D_{H_2O,K}, \quad D^{eff}_{O_2,K} = \frac{\varepsilon}{\tau} D_{O_2,K} \tag{17}$$

τ is the tortuosity factor of porous electrodes. D_{i-j} and D_{iK} are the binary and Knudsen diffusivity, respectively.

3.2. Level set-based topology optimization

3.2.1. Formulation

The optimization method employed in this study is briefly introduced in this section. Details of the method can be found in Ref. [21]. D is a fixed design domain consisting of the electrolyte and cathode and the corresponding area is marked in Fig. 2. We define the level set function, $\psi(\boldsymbol{x})$, as

$$\begin{cases} 0 < \psi(\boldsymbol{x}) \le 1 & \text{if} \quad \forall \boldsymbol{x} \in \Omega \backslash \partial\Omega \\ \psi(\boldsymbol{x}) = 0 & \text{if} \quad \forall \boldsymbol{x} \in \partial\Omega \\ -1 \le \psi(\boldsymbol{x}) < 0 & \text{if} \quad \forall \boldsymbol{x} \in D \backslash \Omega \end{cases} \tag{18}$$

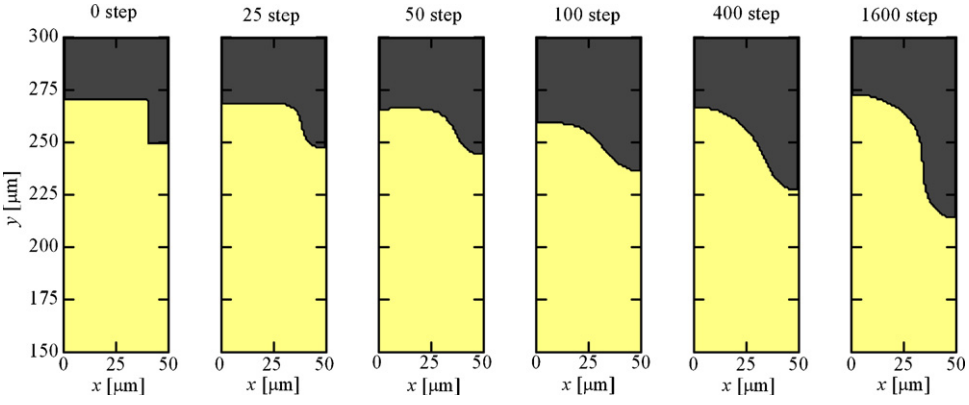

Fig. 6. Evolution of the cathode–electrolyte interface during optimization calculations.

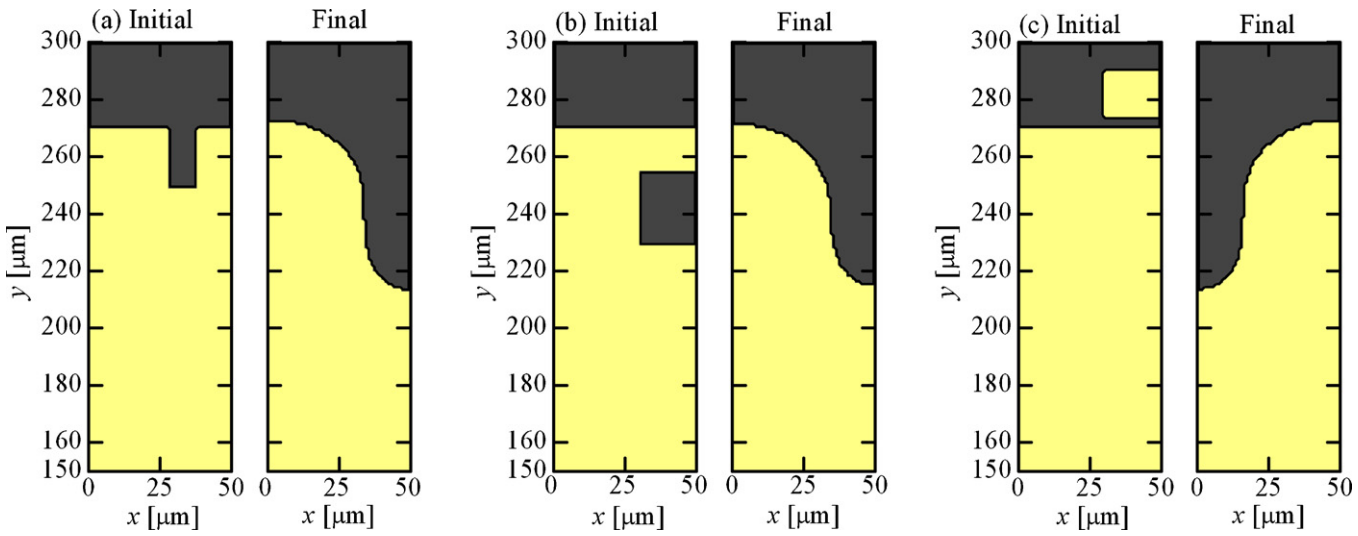

Fig. 8. Influence of the initial configuration upon optimization results.

Positive values of $\psi(\boldsymbol{x})$ correspond to the cathode area, negative values to the electrolyte and the interface between the electrolyte and the cathode is expressed by lines where $\psi(\boldsymbol{x})=0$. The objective functional, F, and the constraint functional with respect to the volume, G, are defined as

$$F(\Omega(\psi)) = \int_{\Omega} f(\boldsymbol{x})d\Omega \tag{19}$$

$$G(\Omega(\psi)) = \int_{\Omega} d\Omega - V_{\max} \le 0 \tag{20}$$

$V_{\max}$ is the upper limit of the volume constraint. We replace this optimization problem with an optimization problem to minimize the energy functional, which is the sum of the fictitious interface energy and the objective functional, formulated as follows:

$$F_R(\Omega(\psi), \psi) = \int_{\Omega} f(\boldsymbol{x})d\Omega + \int_D \frac{1}{2}\gamma\left|\nabla\psi\right|^2 d\Omega \tag{21}$$

$$G(\Omega(\psi)) = \int_{\Omega} d\Omega - V_{\max} \le 0 \tag{22}$$

where F_R is a regularized objective functional and γ is a regularization parameter representing the ratio of the fictitious interface energy and the objective functional. The regularization parameter is possible to adjust the degree of complexity of the optimized structures and sometimes called as the "complexity parameter".

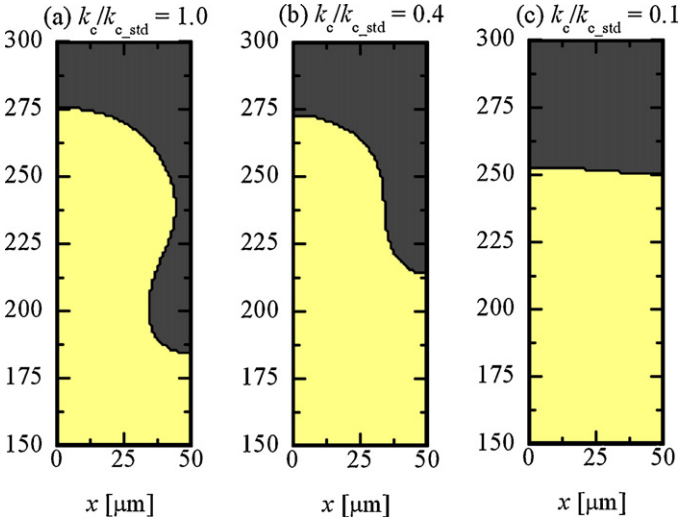

Fig. 9. Influence of O_2 diffusivity upon optimization results, $\gamma = 0.02$.

The optimization problem represented by Eqs. (21) and (22) is replaced with an optimization problem without constraints using Lagrange's method of undetermined multipliers. That is, when the Lagrangian is defined as $\bar{F}_R$ and the Lagrange multiplier of the volume constraint is λ, the optimization problem represented by Eqs. (21) and (22) is replaced with

$$\begin{aligned}\bar{F}_R(\Omega(\psi), \psi) \quad &= \int_{\Omega} (f(\boldsymbol{x}) + \lambda)d\Omega - \lambda V_{\max} + \int_D \frac{1}{2}\gamma|\nabla\psi|^2 d\Omega \\ &\int_{\Omega} (\bar{f}(\boldsymbol{x})d\Omega - \lambda V_{\max} + \int_D \frac{1}{2}\gamma|\nabla\psi|^2 d\Omega\end{aligned} \tag{23}$$

We also assume that level set function changes are proportional to the gradient of Lagrangian $\bar{F}_R$, based on the concept of the phase field method, as shown in the following,

$$\frac{\partial\psi}{\partial t} = -K(\psi)\frac{\delta\bar{F}_R}{\delta\psi} \tag{24}$$

where $K(\psi) > 0$ is a constant of proportion. Substituting Eq. (23) into Eq. (24), we have

$$\frac{\partial\psi}{\partial t} = -K(\psi)(D_T\bar{F} - \gamma\nabla^2\psi) \tag{25}$$

where $D_T\bar{F}$ is a topological derivatives with respect to the Lagrangian $\bar{F}_R$. The Lagrange multiplier is expressed as

$$\lambda = -\frac{\int_{\Omega} K(\psi)(D_T\bar{F} + \gamma\nabla^2\psi)d\Omega}{\int_{\Omega} K(\psi)d\Omega} \tag{26}$$

To represent the level set function independent of the exterior of the fixed design domain D, we assume that the boundary condition of the level set function obeys a Dirichlet boundary condition on the non-design boundary, and a Neumann boundary condition on the other boundaries. The system of the time evolutional equation can then be represented as

$$\begin{cases} \dfrac{\partial\psi}{\partial t} = -K(\psi)(D_T\bar{F} - \gamma\nabla^2\psi) \\ \dfrac{\partial\psi}{\partial n} = 0 \quad \text{on} \quad \partial D\backslash\partial D_N \\ \psi = 1 \quad \text{on} \quad \partial D_N \end{cases} \tag{27}$$

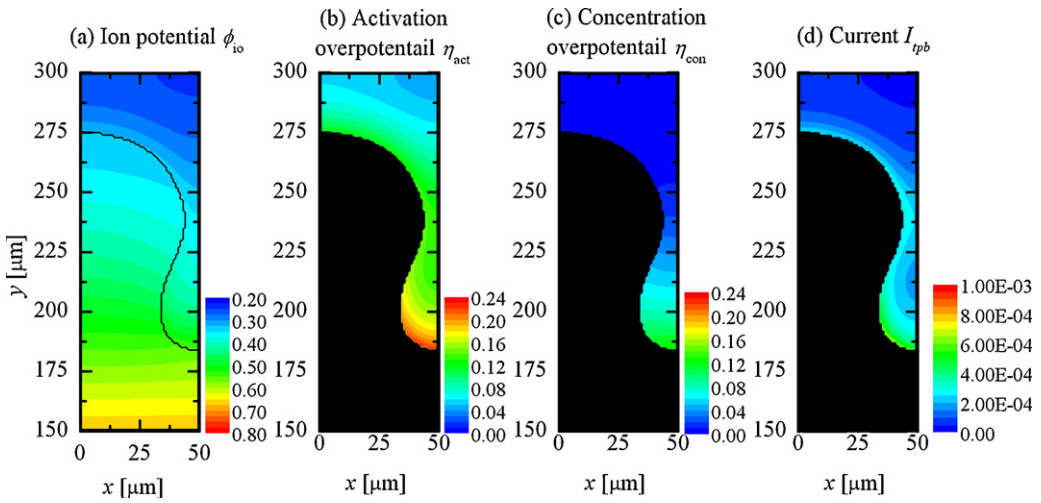

Fig. 10. Ion potential, activation overpotential, concentration overpotential and three-phase boundary charge transfer current for optimal configuration, $k_c/k_{c\_std} = 1.0$, $\gamma = 0.02$.

3.2.2. Application to SOFC simulation

The design domain includes the cathode and upper half of the electrolyte, as shown in Fig. 3. As mentioned above, a Dirichlet boundary condition is set at the cathode surface while a Neumann boundary condition is applied to the other boundaries. The apparent average current density is expressed as

$$i_{ave} = \frac{\int_\Omega i_{tpb} l_{tpb} d\Omega}{S_{cathode}} \tag{28}$$

$S_{cathode}$ is the cathode surface area within the computational domain. We set the objective functional $F(\Omega(\psi))$ as below and consider an optimization problem to maximize the total current under a given terminal voltage.

$$f(\boldsymbol{x}) = -i_{tpb} l_{tpb} \tag{29}$$

$$F(\Omega(\psi)) = -\int_\Omega i_{tpb} l_{tpb} d\Omega \tag{30}$$

The Lagrangian is expressed as

$$\bar{F} = \int_\Omega (f(\boldsymbol{x}) + \lambda) d\Omega = \int_\Omega (-i_{tpb} l_{tpb} + \lambda) d\Omega \tag{31}$$

Ionic conductivity and the gas diffusion coefficient are given as

$$\sigma_{io} = \sigma_C H(\psi) + \sigma_E (1 - H(\psi)) \tag{32}$$

$$k_{O_2} = k_c H(\psi) \tag{33}$$

$$H(\psi) = \begin{cases} 1 & \text{at cathode} \\ 0 & \text{at electrolyte} \end{cases} \tag{34}$$

where σ_C and σ_E are the effective ionic conductivity in the cathode and the ionic conductivity of the electrolyte, respectively. The maximum volume of the cathode is set so that the average cathode thickness does not exceed 50 μm. This is equivalent to ensure the minimum average electrolyte thickness of 200 μm. To avoid an artificial formation of electrolyte inside the cathode, the following condition is applied inside the cathode.

$$\bar{f}(\boldsymbol{x}) = 0 \quad \text{if} \quad \bar{f}(\boldsymbol{x}) < 0 \tag{35}$$

The flowchart of the simulation is shown in Fig. 5.

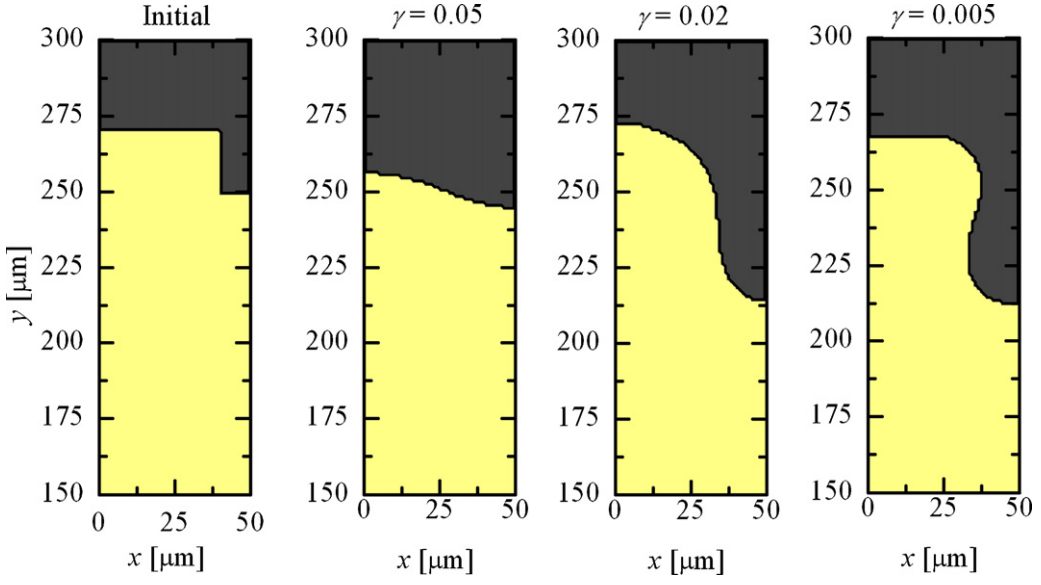

Fig. 11. Influence of the complexity parameter upon optimization results ($k_c/k_{c\_std} = 0.4$).

3.3. Computational conditions

The cell is assumed to operate under atmospheric pressure at a constant and uniform operation temperature of 800 °C. The fuel supplied to the anode surface is humidified hydrogen, the gas composition of which is H_2:H_2O = 0.99:0.01. On the cathode surface, dry oxygen diluted with nitrogen is supplied. The cathode gas composition is O_2:N_2 = 0.05:0.95. The anode and cathode electronic potentials are given as the boundary conditions for calculations of the equivalent circuit. We applied the Nernst potential to the anode while the cell terminal voltage was applied to the cathode. The Nernst potential is calculated as

$$\phi_0 = E_0 + \frac{RT}{2F} \ln \left(\frac{p_{H_2,\infty}}{p_{H_2O,\infty}} \left(\frac{p_{O_2,\infty}}{10,130} \right)^{0.5} \right) \quad (36)$$

where E_0 is the electromotive force at the standard state. Symmetric boundary conditions are applied to the vertical boundaries in the x-direction in Fig. 3.

4. Simulation results and discussion

4.1. General features of optimization calculation

4.1.1. Example of optimizing process

Fig. 6 shows a typical example of the shape evolution during optimization calculations. The thick gray region represents the cathode area. Changes in the average current density and Lagrangian during these particular calculations are shown in Fig. 7. The step number in the figures indicates the number of times the level set function has been updated. Step 0 is the initial state. Right after the calculation starts, the dividing line between the cathode and the electrolyte gradually moves as shown in Fig. 6. The volume of the cathode increases until the step number reaches approximately 100 when a sudden change in the Lagrangian is observed, as shown in Fig. 7. This is when the cathode reaches the upper limit of the volume constraint. The dividing line continues to evolve after step number 100 but the volume of the cathode (or electrolyte) is kept constant. The shape of the interface is almost stable after step number 1200, corresponding well with the almost constant average current density after step 1200 observed in Fig. 7. The average current density is increased from its initial value of 678 mA cm^{-2} to the final value, 726 mA cm^{-2}, during the calculation process, showing that the level set-based topology optimization method is successfully implemented in this 2D SOFC calculation. To the best of the authors' knowledge, this is the first report of an optimization calculation applied in SOFC simulations.

4.1.2. Effect of initial configuration

To clarify if the results show any dependency on the initial configuration, optimization calculations are conducted for the different initial configurations shown in Fig. 8. The only difference among these calculations is the initial configuration; all other conditions are identical. The final results obtained by the optimization calculations match each other very well, as can be confirmed in Fig. 8. Note that the final result shown in Fig. 8(c) can be considered practically the same as that of Fig. 8(a) and (b) because a symmetric boundary condition is applied in the x-direction for these calculations. The average current density at the final states are 725.60 mA cm^{-2} in all cases. It demonstrates that the present optimization calculation method is independent of the initial configuration.

4.2. Optimization under different conditions

The effects of cathode–electrolyte interface modification on the cell's power generation performance are discussed in this section, based on the numerical results obtained by the optimization calculations. Calculations were conducted for different values of the oxygen diffusivity and complexity parameter.

4.2.1. Effect of oxygen diffusivity

The value of the oxygen diffusivity, k_c, which appears in Eq. (16), is artificially changed to investigate how the gas diffusion affects the optimized geometry. The oxygen diffusivity estimated through the model explained in Section 3.1 is set as the standard value, expressed here as k_{c_std}. Calculations are carried out for different values of the oxygen diffusivity, with k_c/k_{c_std} = 1.0, 0.4 and 0.1. In a real cathode, a change in k_c should be associated with some change of the porous microstructure and therefore other geometric parameters are expected to change simultaneously. In this study, however, such effects are neglected and only the value of k_c is altered.

Fig. 9 shows the shapes of the optimized cathode–electrolyte interface for the three cases calculated. It is obvious that the value of the oxygen diffusivity affects the final results. A deep and large-scale groove is observed when k_c/k_{c_std} = 1.0. The grooved part becomes shallower for smaller values of k_c/k_{c_std} and when k_c/k_{c_std} = 0.1, the interface is almost flat.

To evaluate power generation enhancement, we conducted a calculation for a reference case in which both the cathode and electrolyte shapes are set as flat, with constant and uniform thicknesses of 50 μm and 200 μm, respectively. The value of k_c/k_{c_std} is unity. The other conditions are the same as for the optimization calculations in Fig. 9. The average current density of the reference case is 688 mA cm^{-2}. For the three cases shown in Fig. 9, the average current density is calculated as, 760, 726, and 563 mA cm^{-2} for k_c/k_{c_std} = 1.0, 0.4 and 0.1, respectively. We observe approximately a 10% improvement for k_c/k_{c_std} = 1.0. Even for the case where k_c/k_{c_std} = 0.4, about a 6% improvement is achieved. It is worth noting that the improvement in the average current density is achieved for the same amount of cathode/electrolyte material, by introducing a non-uniform cathode–electrolyte interface structure. In the case where k_c/k_{c_std} = 0.1, however, the current density is decreased by 18%.

Fig. 10 shows the distributions of the ion potential, activation overpotential, concentration overpotential and charge transfer current in the domain of the optimization calculation for the case where k_c/k_{c_std} = 1.0. The electron potential in the cathode is assumed uniform in this study. Therefore the potential difference between the ion and the electron is large in the region where the ion potential is high. In Fig. 10(a), the ion potential is high at the bottom of the groove. The charge transfer current, I_{tpb}, in Fig. 10(d) takes large value in this region accompanied by high activation loss shown in Fig. 10(b). As a result of intensive oxygen consumption, the concentration overpotential becomes relatively high in the same region. On the other hand at the convex side of the electrolyte, ion potential is relatively low because of the ion transport loss in the dense electrolyte. Therefore the driving force of the reaction is relatively weak compared to the groove bottom. Nevertheless moderate charge transfer current is observed in the vicinity of the interface even at the top region of the convex part where the concentration overpotential is negligible. Consequently the electrochemically active region spreads near the cathode–electrolyte interface.

4.2.2. Effect of complexity parameter

The effects of the complexity parameter, γ in Eq. (21), upon the optimized structure are examined. Optimization calculations

are conducted for three different values of the complexity parameter and the results are shown in Fig. 11. Calculation conditions other than the complexity parameter are the same for the three cases. It is confirmed that different optimization results can be obtained by tuning the value of this parameter. In general, smaller values of the complexity parameter are seen to yield optimal configurations with more "complex" geometry [21]. The shapes presented in Fig. 11 seem to follow this trend, showing a relatively flat cathode–electrolyte interface for the largest value, $\gamma = 0.05$. The average current density is 707, 726 and 694 mA cm^{-2} for $\gamma = 0.005$, 0.02 and 0.05, respectively. The results indicate that cell performance improvement is not a monotonous function of the complexity parameter.

5. Conclusions

To explore potential for the power density enhancement of solid oxide fuel cells by controlling the electrode–electrolyte interface, we performed two-dimensional numerical simulations of a SOFC, where a level set-based topology optimization technique was applied for the local optimization of the interface shape. The following conclusions were obtained.

(1) The level set-based optimization method was successfully coupled with the SOFC simulation based on a microscale model for the first time. The optimization method was applied to the cathode side of a cell to find the optimized shape of the cathode–electrolyte interface that maximizes the current density under a given terminal voltage. Converged solutions were obtained after sufficient iterations. The solutions were confirmed to be independent of the initial conditions.
(2) The numerical results show that the cell performance can be improved by applying non-flat design to the cathode–electrolyte interface for the same amount of cathode/electrolyte materials. In a standard case set in this study, $k_c/k_{c\_std} = 1.0$ and $\gamma = 0.02$, a wavy interface is obtained as an optimized shape. Approximately a 10% improvement of the current density is observed for this case compared to a conventional flat interface. The shape of the interface can be tuned by changing the complexity factor of the optimization calculation.
(3) The numerical results show that the optimized shape of the cathode–electrolyte interface varies depending on the simulation conditions. When the gas diffusion resistance in the cathode is large, the optimized interface tends to become flat. An optimized interface is determined as a result of combined effects of various resistances closely related to the microstructure of the electrode.

Acknowledgments

This work is partially supported by the European Commission (project Dev-BIOSOFC, FP6-042436, MTKD-CT-2006-042436). HI, MS and HY are supported by the New Energy and Industrial Technology Development Organization (NEDO) under the Development of System and Elemental Technology on Solid Oxide Fuel Cell (SOFC) Project. Special thanks go to Mr. Kazufumi Kodani and Mr. Kuniaki Yoshikata (Dai Nippon Pringting Co., Ltd., Japan) for their support in the cell fabrication.

Appendix A. Preliminary experiment with cathode–electrolyte interface modification

The results of the optimization simulation show the possibility of the cell performance enhancement by cathode–electrolyte interface modification in mesoscale. A preliminary experiment is conducted to see the fundamental effects of the interface modification.

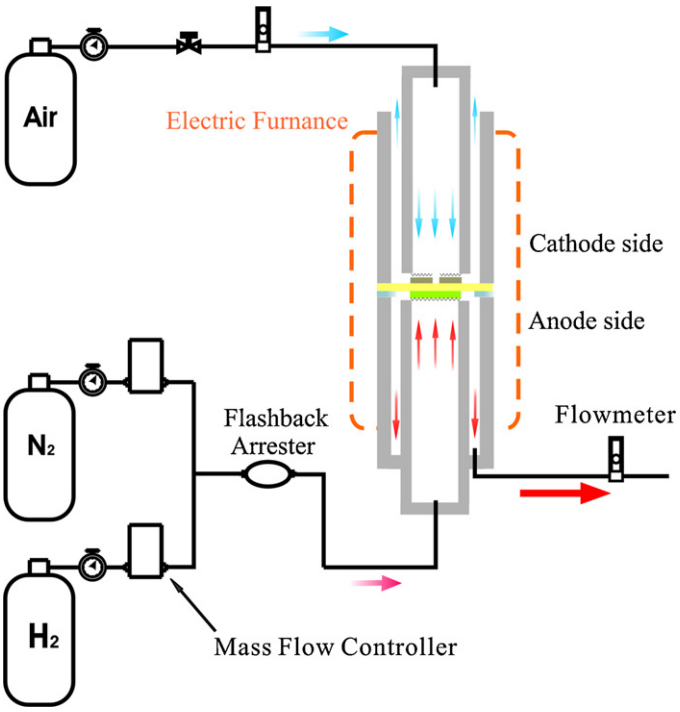

Fig. A1. Overall view of experimental arrangement.

Fig. A1 shows an overview of the experimental apparatus. A button type cell is used. The entire test section is placed in an electric furnace to control the operation temperature. Fig. A2 shows the electrolyte of a test cell, a small disk-shaped YSZ ceramic. The diameter and thickness of the electrolyte are 20 mm and 0.5 mm, respectively. The cathode side surface is partially grooved by applying sandblasting method on the initial flat surface. Two types of groove shape are prepared, and the details of their geometries are summarized in Table A1. The area enlargement factor is defined as the ratio of the electrode–electrolyte interface area of a grooved

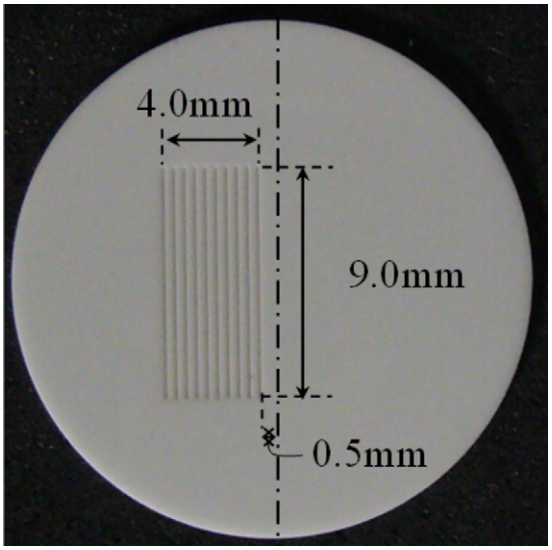

Fig. A2. Top view of cathode side electrolyte with grooves (large grooves).

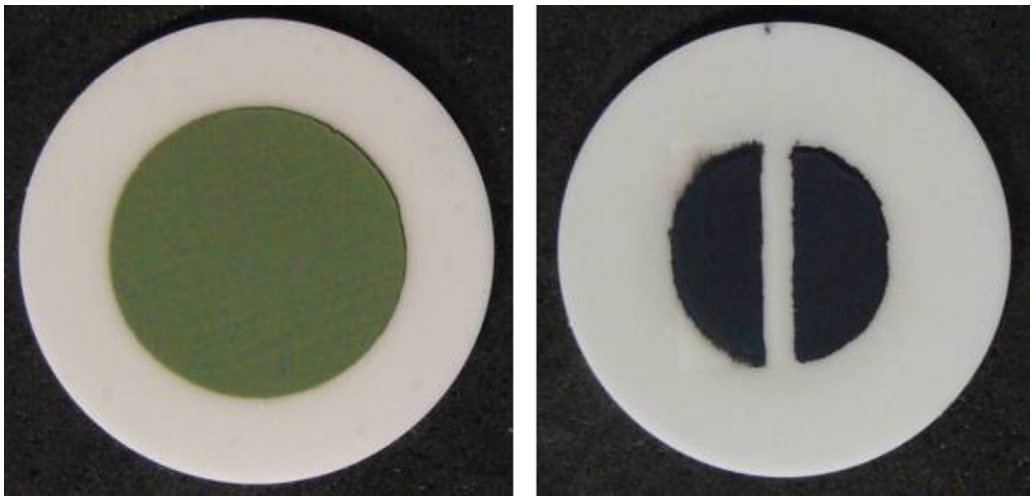

Fig. A3. Anode and cathodes fabricated on a test cell.

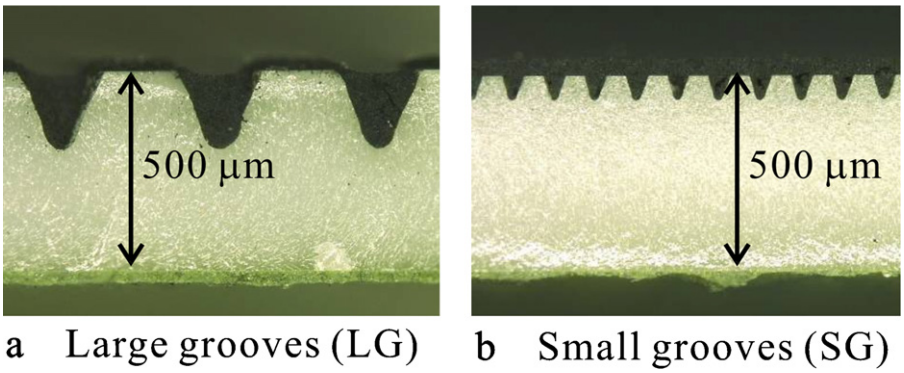

Fig. A4. Cross-section view of grooved portions.

Table A1
Geometric details of the grooves.

	Depth (μm)	Width (μm)	Interval (μm)	Area enlargement factor
Large grooves (LG)	210	210	220	1.58
Small grooves (SG)	60	60	50	1.72

portion to a corresponding flat portion. The electrolyte surface is flat on the anode side.

Electrode materials are prepared following the procedure noted in Ref. [20]. The anode material, NiO–YSZ, is mixed with polyethylene glycol, screen printed on the electrolyte and sintered at 1400 °C for 5 h. The cathode material, LSM, is also mixed with polyethylene glycol to form slurry, which is screen printed on the electrolyte and sintered at 1150 °C for 5 h. As can be seen in Fig. A3(b), the cathode is segmented into two parts. One side covers the flat surface and the other covers the grooved surface. LSM cathode is used because the effect of the grooves is expected to be prominent when the electrochemical reaction takes place only in the vicinity of the interface. Considering that the ionic conductivity of LSM is small, LSM cathode is expected to maximize the difference between the two-segmented cathodes. Fig. A4 shows cross-sectional views of the grooves for the two types of cell. Power generation tests using each part of the cathode are conducted individually to obtain the *i*–*V* characteristics and results are compared. The current density, *i*, is defined as the measured current divided by the projected cathode area. The projected area is evaluated through image processing. The experiments were conducted at various operating temperatures (800, 850 and 900 °C).

Fig. A5 compares the *i*–*V* curves obtained from two cathodes with and without the grooves at different temperature. Dry hydrogen is supplied to the anode side as fuel while dry air is supplied to the cathode side. The current density obtained from the cathode with grooves is always larger than that from the flat cathode in both groove sizes (LG or SG) when it is compared at the same terminal voltage. Fig. A5 shows an experimental example where the cell performance is enhanced by the cathode–electrolyte interface modification. If the current density at the terminal voltage of 0.6 V is compared, the cathode with grooves achieves approximately 30–40% larger value than the flat cathode. This is less than the area enlargement factor in Table A1. As discussed with the simulation results, the cell performance is affected by many factors, local ion potential, local electron potential and gas composition, etc. The degree of enhancement by the interface modification is determined as a result of the combination effects of those factors. To clarify each effect in experiments is an important work left for future investigation.

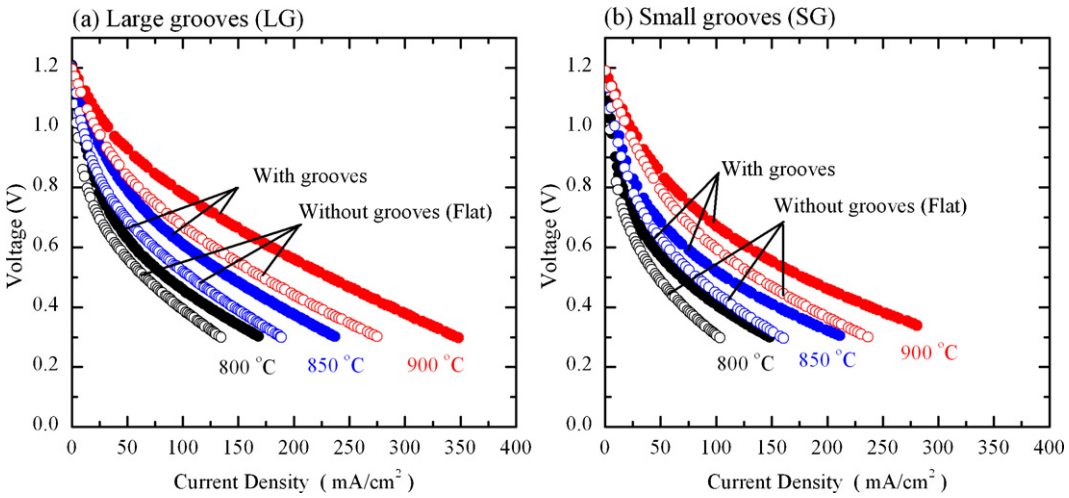

Fig. A5. *i*–*V* characteristics of the cells with segmented cathodes. In each cell, one cathode is fabricated on the grooved electrolyte with the other cathode on the flat electrolyte.

References

[1] S.C. Singhal, K. Kendall, High Temperature Solid Oxide Fuel Cells, Elsevier, 2002.
[2] S.C. Singhal, Solid State Ionics 135 (2000) 305–313.
[3] J.-H. Kim, R.-H. Song, K.-S. Song, S.-H. Hyun, D.-R. Shin, H. Yokokawa, J. Power Sources 122 (2003) 138–143.
[4] N.M. Sammes, Y. Du, R. Bove, J. Power Sources 145 (2005) 428–434.
[5] T. Suzuki, T. Yamaguchi, Y. Fujishiro, M. Awano, J. Power Sources 160 (2006) 73–77.
[6] H. Koide, Y. Someya, T. Yoshida, T. Maruyama, Solid State Ionics 132 (2000) 253–260.
[7] A. Atkinson, S. Barnett, R.J. Gorte, J.T.S. Irvine, A.J. Mcevoy, M. Mogensen, S.C. Singhal, J. Hohs, Nat. Mater. 3 (2004) 17–27.
[8] H. Abe, K. Murata, T. Fukui, W.-J. Moon, K. Kaneko, M. Naito, Thin Solid Films 496 (2006) 49–52.
[9] T. Fukui, K. Murata, S. Ohara, H. Abe, M. Naito, K. Nogi, J. Power Sources 125 (2004) 17–21.
[10] H. Itoh, T. Yamamoto, M. Mori, T. Horita, N. Sakai, H. Yokokawa, M. Dokiya, J. Electrochem. Soc. 144 (1997) 641–646.
[11] H. Iwai, N. Shikazono, T. Matsui, H. Teshima, M. Kishimoto, R. Kishida, D. Hayashi, K. Matsuzaki, D. Kanno, M. Saito, H. Muroyama, K. Eguchi, N. Kasagi, H. Yoshida, J. Power Sources 195 (2010) 955–961.
[12] M. Kishimoto, H. Iwai, M. Saito, H. Yoshida, Proceedings of the 14th International Heat Transfer Conference, IHTC14-22495, 2010.
[13] T. Tsai, S.A. Barnett, Solid State Ionics 93 (1997) 207–217.
[14] T.W. Eom, H.K. Yang, K.H. Kim, H.H. Yoon, J.S. Kim, S.J. Park, Ultramicroscopy 108 (2008) 1283–1287.
[15] S.D. Kim, S.H. Hyun, J. Moon, J.-H. Kim, R.H. Song, J. Power Sources 139 (2005) 67–72.
[16] T. Kenjo, M. Nishiya, Solid State Ionics 57 (1992) 295–302.
[17] E.P. Murray, T. Tsai, S.A. Barnett, Solid State Ionics 110 (1998) 235–243.
[18] V.A.C. Haanappel, J. Mertens, D. Rutenbeck, C. Tropartz, W. Herzhof, D. Sebold, F. Tietz, J. Power Sources 141 (2005) 216–226.
[19] W.Z. Zhu, S.C. Deevi, Mater. Sci. Eng. A362 (2003) 228–239.
[20] A. Konno, H. Iwai, K. Inuyama, A. Kuroyangagi, M. Saito, H. Yoshida, K. Kodani, K. Yoshikata, J. Power Sources, in press.
[21] T. Yamada, K. Izui, S. Nishiwaki, A. Takezawa, Comput. Methods Appl. Mech. Eng., in press.
[22] T. Kenjo, S. Osawa, K. Fujikawa, J. Electrochem. Soc. 138 (1991) 349–355.
[23] S. Sakamoto, H. Taira, H. Takagi, Denki Kagaku 64 (1996) 609–613.
[24] N.F. Bessette II, W.J. Wepfer, J. Winnick, J. Electrochem. Soc. 142 (11) (1995) 3792–3800.
[25] P. Costamagna, K. Honegger, J. Electrochem. Soc. 145 (1998) 3995–4007.
[26] J.H. Nam, D.H. Jeon, Electrochim. Acta 51 (2006) 3446–3460.
[27] A. Bieberle, L.P. Meier, L.J. Gauckler, J. Electrochem. Soc. 148 (2001) 646–656.
[28] R. Radhakrishnan, A.V. Virkar, S.C. Singhal, J. Electrochem. Soc. 152 (2005) 210–218.
[29] U. Anselmi-Tamburini, G. Chiodelli, M. Arimondi, F. Maglia, G. Spinolo, Z.A. Munir, Solid State Ionics 110 (1998) 35–43.
[30] J.R. Ferguson, J.M. Fiard, R. Herbin, J. Power Sources 58 (1996) 109–122.
[31] E.A. Mason, A.P. Malinauskas, R.B. Evans III, J. Chem. Phys. 46 (1967) 3199–3216.
[32] D. Arnost, P. Schneider, Chem. Eng. J. 51 (1995) 91–99.
[33] R. Suwanwarangkul, E. Croiset, M.W. Fowler, P.L. Douglas, E. Entchev, M.A. Douglas, J. Power Sources 122 (2003) 9–18.
[34] H. Zhu, R.J. Kee, J. Power Sources 117 (2003) 61–74.
[35] S.H. Chan, K.A. Khor, Z.T. Xia, J. Power Sources 93 (2001) 130–140.